JOURNAL OF SPACECRAFT AND ROCKETS
Vol. 46, No. 6, November–December 2009

Influence of Asymmetric Transition Conditions on a Slender-Body Flight Vehicle

Seol Lim*
Yeungnam University, Gyeongsan 712-749, Republic of Korea
Sang Dug Kim†
UNISON Company, Ltd., Gyeongsan 664-942, Republic of Korea
and
Dong Joo Song‡
Yeungnam University, Gyeongsan 712-749, Republic of Korea

DOI: 10.2514/1.40665

The flow characteristics of asymmetric vortices and the side force of a tangent-ogive-cylinder flight vehicle at high angles of attack have been studied by using a three-dimensional upwind Navier–Stokes method with the k-ω turbulence model and a simple laminar–turbulent transition model. Various patterns of asymmetric vortices and side forces are studied by using various asymmetric laminar–turbulent transition conditions. Asymmetrically changing turbulent viscosities that arise from asymmetric laminar–turbulent transition conditions cause asymmetric crossflow vortex structures and side forces at higher angles of attack. The magnitude and structure of the crossflow vortices and side forces were sensitive to changes in the factors of the model of laminar–turbulent transition.

Nomenclature

C_N = overall normal-force coefficient [overall normal force divided by $(q\pi D^2/4)$]
C_Y = overall side-force coefficient [overall side force divided by $(q\pi D^2/4)$]
C_{YL} = local side-force coefficient [local side force divided by $(qD\sin^2\alpha)$]
D = cylinder diameter
L_n = length of the nose part
Ma = Mach number
q = freestream dynamic pressure
R = cylinder radius
Re_D = Reynolds number, UD/ν
x = axial distance from the nose tip
α = angle of attack
ν = kinematic viscosity
ν_T = turbulent viscosity in the fully turbulent region
ν_{TR} = turbulent viscosity in the transition region

I. Introduction

THE flight capacities of recent fighters and missiles have been extended to satisfy the increased demand for greater maneuverability. The demand for greater maneuverability requires flight through conditions of high angles of attack. At high angles of attack, the flow structure around a slender-body shape, such as a missile or the forebody part of a fighter, is characterized by various conditions of flow separation. Figure 1 shows four distinct regimes of the flow structure that surrounds a slender missile or the forebody part of a fighter. As the angle of attack is increased from 0 to 90 deg, these flow-structure regimes include: vortex-free flow, symmetric vortex-flow, steady asymmetric vortex-flow, and wakelike flow [1,2].

Under an asymmetric vortex-flow regime at high angles of attack, the flow separation and the vortex induce a large, unwanted, side force which greatly affects flight stability even at a zero angle of the sideslip. Many researchers have observed this unwanted side force through experimental investigations and termed it a phantom yaw. These large side forces and asymmetric flow separations show very irregular patterns that vary with the prevailing conditions. Thus, it is difficult to find out the reasons for and the flow structures of these phenomena. The causes of these large side forces and asymmetric flow separations are thought to be micro asymmetries on the surface that result from microscopic imperfections and the uneven conditions of external-flow characteristics. It is well known that asymmetric separations and large side forces are affected by the Reynolds number, the shape of the forebody, and the angle of attack. Large, unwanted, side forces that result from asymmetric separations and vortices decrease the flight vehicle's overall performance and limit flight domains. Thus, additional methods for yaw control might be required for stable vehicle operation [3–6].

Through many experimental studies, the existence and trend of the phantom yaw has been ascertained. For practical research, computational fluid dynamics (CFD) methods can be considered. In prior numerical studies, various features (e.g., artificially asymmetric geometry, sideslip angle, and rolling) were used to describe the steady asymmetric vortex and the side force at high angles of attack. However, these approaches include artificial modifications of the geometry and flow conditions. As a result, many difficulties arise with regard to the application of these approaches to real and practical problems. In this study, the method of using artificial and asymmetric laminar–turbulent transition conditions is suggested for describing the steady asymmetric vortex and the side force at high angles of attack. This approach does not include modifications of the flight vehicle geometry and flow conditions.

The work of Chin et al. [7] showed the asymmetric side force consistent with available data by using slender-body theory and discrete vortex model with separation-point and vortex-free conditions. They assumed the flow is conical, so that the separation lines are straight. They specified the separation lines from experiment or boundary-layer calculation. The side-force coefficients at zero-sideslip condition for the cone and the tangent ogive were similarly predicted reasonably well with the available data. In this study, artificially generated asymmetric turbulent viscosity by asymmetric

Presented as Paper 4071 at the 38th Fluid Dynamics Conference and Exhibit, Seattle, WA, June 2008; received 23 March 2009; revision received 4 Aug. 2009; accepted for publication 17 Aug. 2009.

*Research Assistant, School of Mechanical Engineering. Student Member AIAA.
†Team Manager, Wind Energy Research & Development Center. Member AIAA.
‡Professor, School of Mechanical Engineering. Member AIAA.

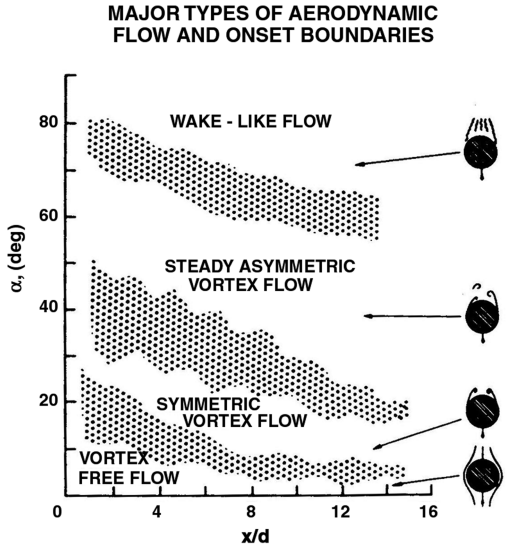

Fig. 1 Angle-of-attack boundaries that separate the four major types of cross-sectional aerodynamic flow pattern for pointed bodies [1].

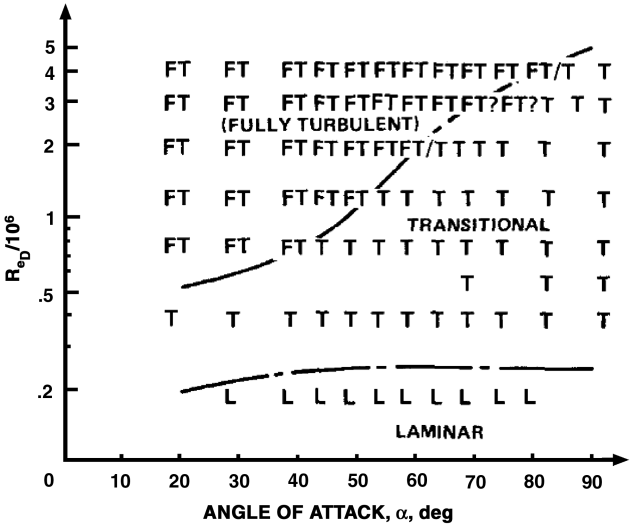

Fig. 2 Classification of the results into three main flow regimes (Lamont [8]).

laminar–turbulent transition condition may cause similar structure of flow separation and vortex.

Through several experimental studies, it is well known that the asymmetric vortex and the side force are closely related to the Reynolds number. The laminar-, transitional-, and turbulent-flow regimes with respect to angles of attack are classified by Lamont (Fig. 2) [8]. It is well-known that the maximum side force is often found in the regime of the laminar–turbulent transition of flow (Fig. 3) [9,10].

II. Numerical Method

A. Flowfield Analysis

The 3-D conservative supracharacteristics method (CSCM) [11] compressible upwind flux-difference-splitting Navier–Stokes method with the k-ω turbulence model [12] is used to compute the flowfields. The current computational method was extensively used by current authors [12–16].

Asymmetric laminar–turbulent transition conditions are set on the surface of the flight vehicle to generate an asymmetric vortex along the vehicle. An message passing interface library and a PC-cluster system are used to reduce the computational time.

A finite difference formulation of the compressible Navier–Stokes equations with a two-equation turbulence model can be expressed as

$$\frac{\partial q}{\partial t}+\frac{\partial E}{\partial x}+\frac{\partial F}{\partial y}+\frac{\partial G}{\partial z}=\frac{\partial E_v}{\partial x}+\frac{\partial F_v}{\partial y}+\frac{\partial G_v}{\partial z}+S \tag{1}$$

In Eq. (1), the conservative dependent variables are q; the inviscid fluxes E, F, and G; the viscous fluxes, E_v, F_v, and G_v; and the turbulence-source term S.

The CSCM upwind flux-difference-splitting method uses the properties of similarity transformation with reference to the conservative, primitive, and characteristic variables:

$$\begin{aligned}\Delta F &= A\Delta q=\bar{M}\,\bar{T}\,\Lambda\bar{T}^{-1}\bar{M}^{-1}\Delta q=\bar{M}\,\bar{T}\,\Lambda\bar{T}^{-1}\Delta\tilde{q}\\ &=\bar{M}\bar{A}'\Delta\tilde{q}=\bar{M}\,\bar{T}\,\Lambda\bar{T}^{-1}\Delta\tilde{\tilde{q}}\end{aligned} \tag{2}$$

In Eq. (2), $\bar{}$ is the simple average of the space; $\tilde{q}$ and $\tilde{\tilde{q}}$ are primitive and characteristic variables, respectively; Λ is a diagonal matrix for

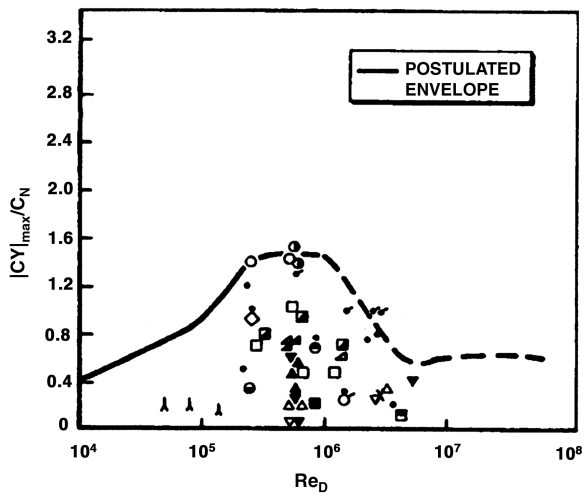

a) Ericsson and Reding [9]

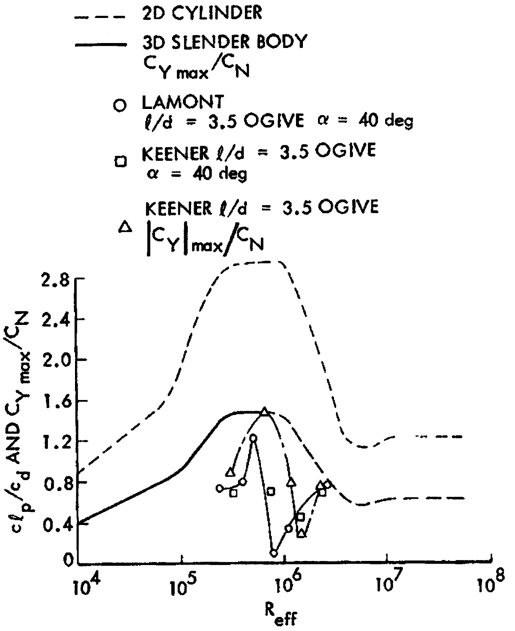

b) Reding and Ericsson [10]

Fig. 3 Maximum values of $|C_Y|/C_N$ as a function of the Reynolds number.

Table 1 Factors and variables for transition model

C_1	−0.412
C_2	0.1
Tu_t	Turbulence intensity at starting position of laminar–turbulent transition
s_t	Starting position of laminar–turbulent transition
λ	Length of laminar–turbulent transition region

which the diagonal elements correspond to the eigenvalues; and the variables q, $\tilde{q}$, and $\tilde{\tilde{q}}$, are related to each other as follows:

$$\Delta\tilde{q} = \bar{M}^{-1}\Delta q, \qquad \Delta\tilde{\tilde{q}} = \bar{T}^{-1}\Delta\tilde{q} \tag{3}$$

The $\bar{M}^{-1}$ matrix transforms conservative into primitive variables. $\bar{T}^{-1}$ is a matrix that transforms primitive into characteristic variables and is chosen somewhat arbitrarily as to the scaling that leads to logarithmic-difference approximations for the density, pressure, and Mach number.

The characteristic variables can be obtained from the primitive variables through the following relation:

$$\bar{T}^{-1}(\bar{A}'\Delta\tilde{q}) = \bar{T}^{-1}(\bar{T}\Lambda\bar{T}^{-1}\Delta\tilde{q}) = \Lambda\Delta\tilde{\tilde{q}} \tag{4}$$

The inviscid flux ΔF can be divided into ΔF^+ and ΔF^- by using the diagonal truth function matrix $D^{\pm}$. Equation (2) can be written as

$$\Delta F = \bar{M}\,\bar{T}(D^+ + D^-)\bar{T}^{-1}\bar{A}'\Delta\tilde{q} = \Delta F^+ + \Delta F^- \tag{5}$$

In Eq. (5),

$$D^+ = \frac{1}{2}\left[\frac{\Lambda}{|\Lambda|} + 1\right]$$

and

$$D^- = \frac{1}{2}\left[\frac{\Lambda}{|\Lambda|} - 1\right]$$

Using the relation $\bar{A}'\Delta\tilde{q} = \tilde{M}^{-1}\Delta q$ the preceding equation can be rewritten as

$$\Delta F^{\pm} = \bar{M}\,\bar{T}\,D^{\pm}\bar{T}^{-1}\tilde{M}^{-1}\Delta\tilde{q} = \tilde{A}^{\pm}\Delta q \tag{6}$$

Equation (6) satisfies the U property of Roe [17] and thus the flux vectors are conserved. Although the formulation becomes complicated due to the transformation matrices $\bar{M}$, $\bar{T}$, and $\tilde{M}^{-1}$, the differencing scheme captures the convective-flow propagation through these matrices and naturally allows tractable, characteristic boundary conditions via the modified T^{-1}.

B. Asymmetric Turbulent Transitions

In this study, a simple laminar–turbulent transition model is used to generate an asymmetric vortex and a side force. The turbulent viscosity in the transition region is modeled by using the turbulent viscosity as calculated by the k-ω turbulence model and the control function F_s, as shown in Eq. (7):

$$\nu_{\mathrm{TR}} = F_s \times \nu_T \qquad (0 \le F_s \le 1) \tag{7}$$

The control function F_s is based on experimental data that were furnished by Gostelow et al.[18] and is simplified as shown in Eq. (8):

$$F_s = \gamma_s \times f_{\mathrm{mix}} \qquad (\gamma_s = 1.0 - \exp(C_1(s - s_t)^2/\lambda)$$
$$f_{\mathrm{mix}} = C_{\mathrm{mix}} + (1.0 - C_{\mathrm{mix}})\gamma_s^3 \qquad C_{\mathrm{mix}} = C_2 \cdot Tu_t^{0.7}) \tag{8}$$

In reality, the condition of laminar–turbulent transition is sensitive to many factors of the flow and surface conditions. All factors and variables are generally determined by experimentation. However, the focus of this study is not the various causes of laminar–turbulent transition but the effect of laminar–turbulent transition. Therefore, the factors and the variables of laminar–turbulent transition are simply selected as in Table 1 following the study of Gostelow et al. [18].

Figures 4a and 4b show the s direction that is divided from the stagnation position on the flight vehicle. The starting position and the length of the laminar–turbulent transition region with respect to the crossflow direction (s direction) are asymmetrically set to generate an asymmetric flow structure. An asymmetric turbulent viscosity is allowed near the surface of the flight vehicle through these asymmetric laminar–turbulent transition parameters. Thus, the constructed asymmetric turbulent viscosity structure affects the asymmetric flow separations and the large side force.

Table 2 shows different cases of laminar–turbulent transition conditions. These conditions are tested and compared for generating an asymmetric vortex and a side force. Case 1 features further delayed start laminar–turbulent transition conditions than the other cases. Case 2 features earlier start laminar–turbulent transition conditions than the other cases. Cases 3 and 4 feature the same region of fully turbulent conditions. However, case 3 features an asymmetric starting position for the laminar–turbulent transition, whereas case 4 features an asymmetric length for the laminar–turbulent transition region.

Table 2 Laminar–turbulent transition conditions

	Case 1	Case 2	Case 3	Case 4
$S_{t,1}$	$3/8\pi R$	$1/8\pi R$	$2/8\pi R$	$3/8\pi R$
$S_{t,2}$	$4/8\pi R$	$2/8\pi R$	$3/8\pi R$	$3/8\pi R$
λ_1	$2/8\pi R$	$2/8\pi R$	$2/8\pi R$	$1/8\pi R$
λ_2	$2/8\pi R$	$2/8\pi R$	$2/8\pi R$	$2/8\pi R$
$S_{t,1} + \lambda_1$	$5/8\pi R$	$3/8\pi R$	$4/8\pi R$	$4/8\pi R$
$S_{t,2} + \lambda_2$	$6/8\pi R$	$4/8\pi R$	$5/8\pi R$	$5/8\pi R$

Table 3 Test conditions

Angle of attack α	30–60 deg
Re_D	440,000
Mach number	0.3
Air model	Perfect gas

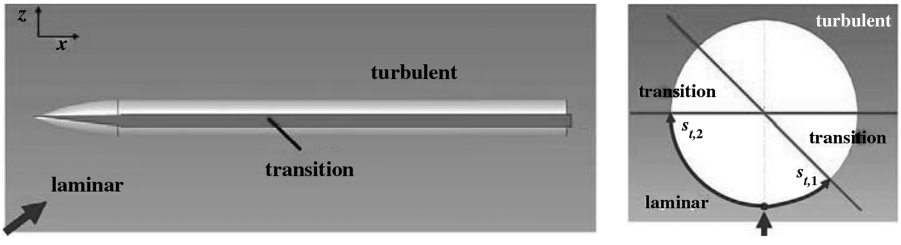

a) Transition region **b) s-directions**

Fig. 4 An example of a generated asymmetric transition region.

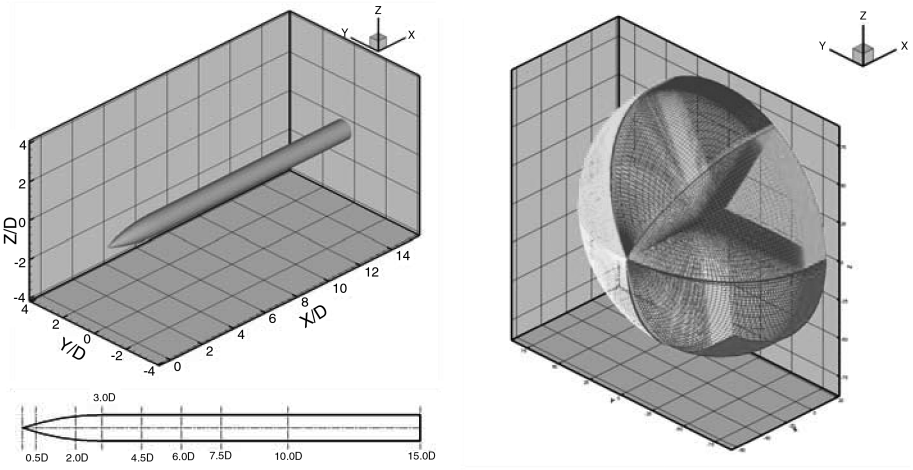

a) Tangent-ogive-cylinder shape b) Grid system (120 x 182 x 120)

Fig. 5 The geometry and the grid system.

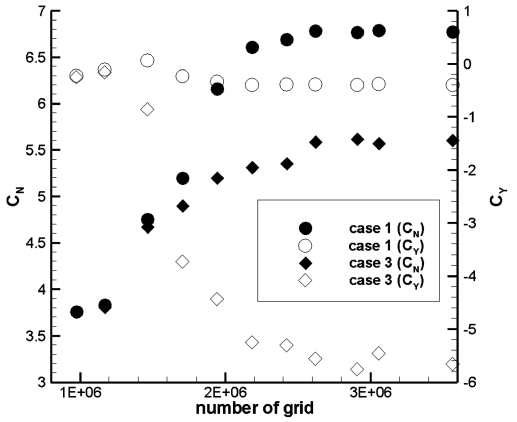

Fig. 6 Grid-convergence test.

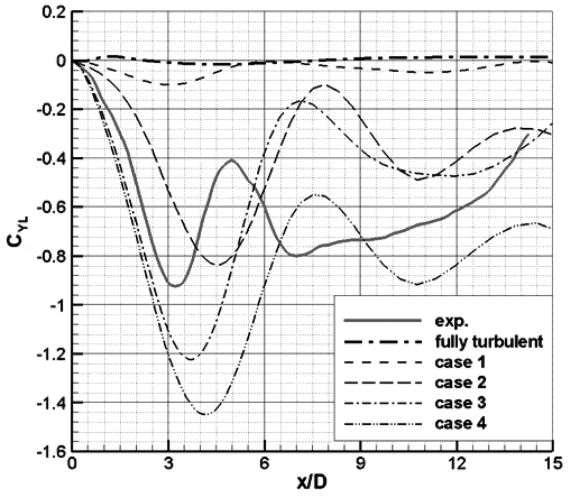

Fig. 7 Comparison of local side-force coefficient distributions: angle of attack = 50 deg.

C. Test and Boundary Conditions

Table 3 shows the test conditions for numerical analysis. The Reynolds number that is based on the base diameter is 440,000 and the angle of attack ranges from 30 to 60 deg. This condition belongs to the transition regime.

The dimensions and details of the tangent-ogive-cylinder model considered here are shown in Fig. 5a. The length of the forebody is 3.0 times the cylinder diameter D and the total length of the flight vehicle is 15.0 D. The grid system is shown in Fig. 5b. For the grid-conversion test (Fig. 6), we tested the grid sensitivity by increasing the grid points from one to three million. Therefore, the final grid system has about 2.6 million grid points and grid points are more numerous in the circumferential direction than in other directions.

III. Results and Discussion

A. Asymmetric Transition Conditions (Angle of Attack = 50 degrees)

Figure 7 shows a comparison of the local side-force coefficient distributions at different laminar–turbulent transition conditions with the experimental data of Champigny [19]. The experimental data and the results from numerical simulation show similar patterns with regard to the local side-force coefficient distribution. In all cases, the maximum local side force appears near the forebody part ($x/D < 3$). After this region, the local side-force distributions fluctuate and exhibit a dwindling trend. The magnitude of local side forces is affected by the asymmetric laminar–turbulent transition conditions. Case 1 features the most delayed fully turbulent condition, under which it is not easy to impact the flow separation. Therefore, case 1 shows lower and more stable values of the local side force than the other cases. Cases 2 and 3 have regions of fully turbulent flow that are developed earlier than in case 1. Therefore, these cases exhibit a greater magnitude of the local side force. Cases 3 and 4 have the same, fully turbulent region but the asymmetric laminar–turbulent transition regions are different. Case 4 has a smaller λ_1 than case 3. This difference can be accompanied by differing magnitudes of the local side force.

Table 4 shows a comparison of the normal- and side-force coefficients across the different cases. Case 3 shows the most similar magnitudes of the normal and the side force, when all the cases are compared with the relevant experimental data. The magnitude of the side force and the trend in the local side-force distribution on the slender body of the flight vehicle are sensitive to changes in the laminar–turbulent transition conditions that can be controlled for this purpose.

Table 4 Comparison of C_N and C_Y: angle of attack = 50 deg

	Exp.	Case 1	Case 2	Case 3	Case 4
C_N	5.6	6.79	4.41	5.59	4.96
C_Y	−6.4	−0.39	−4.11	−5.56	−9.02
$\lvert C_Y\rvert/C_N$	1.14	0.06	0.93	0.99	1.82

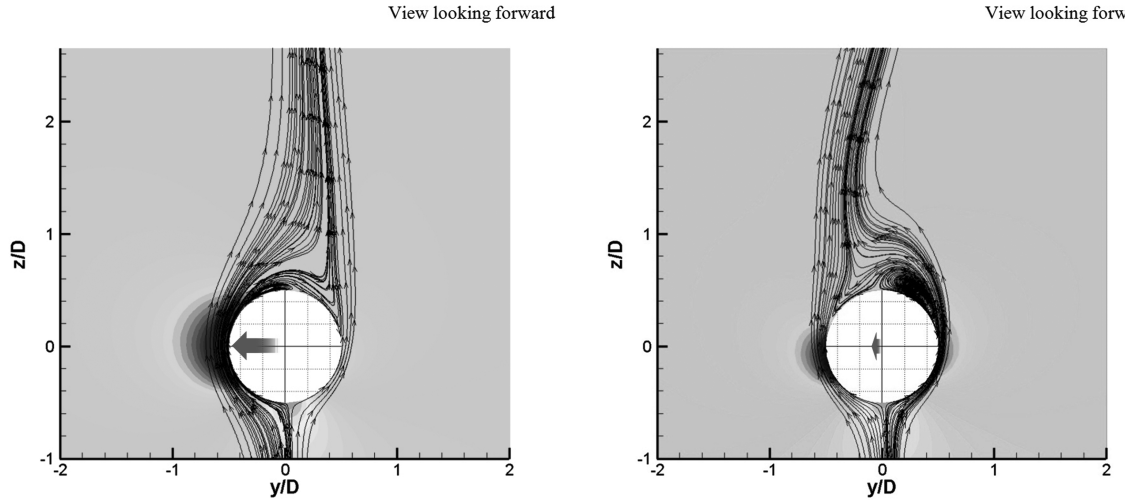

a) x/D=3.5 b) x/D=7.0

Fig. 8 Streamlines and pressure contours at the cross section. Laminar–turbulent transition condition: case 3 angle of attack = 50 deg.

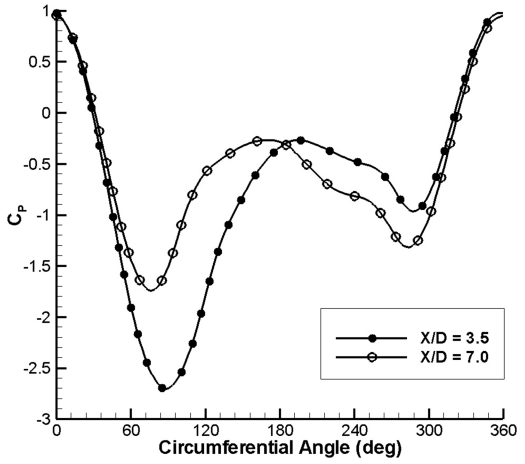

Fig. 9 Circumferential surface pressure distributions. Laminar–turbulent transition condition: case 3 angle of attack = 50 deg.

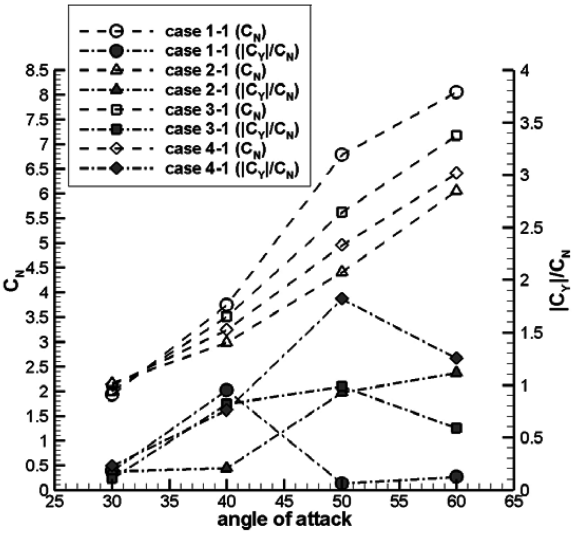

Fig. 11 Comparison of C_N, and $|C_Y|/C_N$.

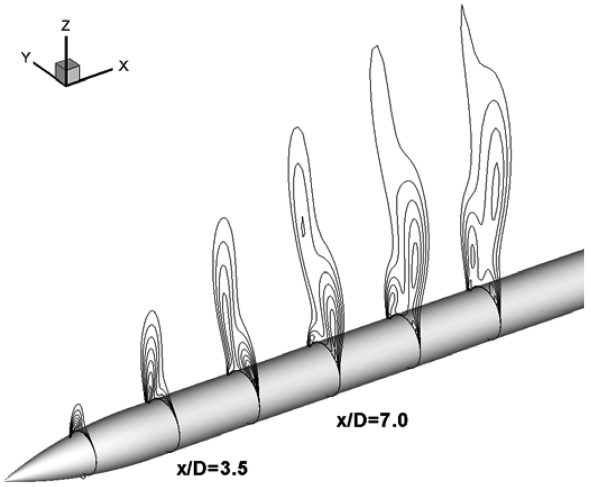

Fig. 10 Total pressure contours. Laminar–turbulent transition condition: case 3 angle of attack = 50 deg.

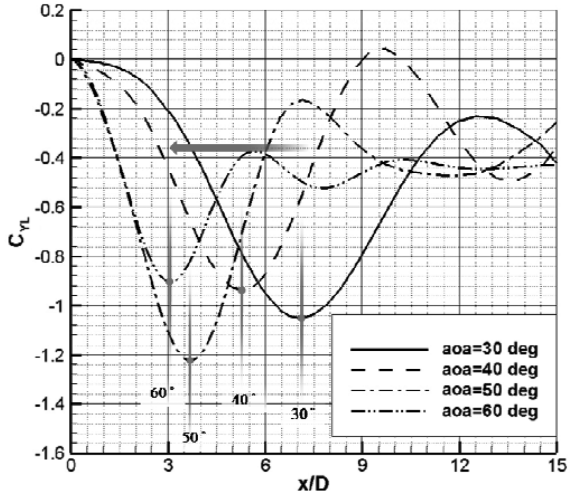

Fig. 12 Comparison of local side-force coefficient distributions. Laminar–turbulent transition condition: case 3-1.

Table 5 Laminar–turbulent transition conditions

	Case 1-1	Case 2-1	Case 3-1	Case 4-1
$S_{t,1}$	$3/8\pi R\frac{\sin(\alpha)}{\sin(50\ \deg)}$	$1/8\pi R\frac{\sin(\alpha)}{\sin(50\ \deg)}$	$2/8\pi R\frac{\sin(\alpha)}{\sin(50\ \deg)}$	$3/8\pi R\frac{\sin(\alpha)}{\sin(50\ \deg)}$
$S_{t,2}$	$4/8\pi R\frac{\sin(\alpha)}{\sin(50\ \deg)}$	$2/8\pi R\frac{\sin(\alpha)}{\sin(50\ \deg)}$	$3/8\pi R\frac{\sin(\alpha)}{\sin(50\ \deg)}$	$3/8\pi R\frac{\sin(\alpha)}{\sin(50\ \deg)}$
λ_1	$2/8\pi R\frac{\sin(\alpha)}{\sin(50\ \deg)}$	$2/8\pi R\frac{\sin(\alpha)}{\sin(50\ \deg)}$	$2/8\pi R\frac{\sin(\alpha)}{\sin(50\ \deg)}$	$1/8\pi R\frac{\sin(\alpha)}{\sin(50\ \deg)}$
λ_2	$2/8\pi R\frac{\sin(\alpha)}{\sin(50\ \deg)}$	$2/8\pi R\frac{\sin(\alpha)}{\sin(50\ \deg)}$	$2/8\pi R\frac{\sin(\alpha)}{\sin(50\ \deg)}$	$2/8\pi R\frac{\sin(\alpha)}{\sin(50\ \deg)}$
$S_{t,1}+\lambda_1$	$5/8\pi R\frac{\sin(\alpha)}{\sin(50\ \deg)}$	$3/8\pi R\frac{\sin(\alpha)}{\sin(50\ \deg)}$	$4/8\pi R\frac{\sin(\alpha)}{\sin(50\ \deg)}$	$4/8\pi R\frac{\sin(\alpha)}{\sin(50\ \deg)}$
$S_{t,2}+\lambda_2$	$6/8\pi R\frac{\sin(\alpha)}{\sin(50\ \deg)}$	$4/8\pi R\frac{\sin(\alpha)}{\sin(50\ \deg)}$	$5/8\pi R\frac{\sin(\alpha)}{\sin(50\ \deg)}$	$5/8\pi R\frac{\sin(\alpha)}{\sin(50\ \deg)}$

B. Flow Characteristics at an Asymmetric Laminar–Turbulent Transition Condition

Figure 8 shows streamlines and pressure contours at the cross section of the axial positions $x/D = 3.5$ and 7.0. The axial position $x/D = 3.5$ is near the position of the maximum local side force and $x/D = 7.0$ is near the position of the minimum local side force. Case 3 describes the asymmetric laminar–turbulent transition condition and an angle of attack of 50 deg.

In the flow characteristics near the position of the maximum local side force (Fig. 8a $x/D = 3.5$), the flow separations at the left and right sides show a considerably asymmetric aspect. Further, the streamlines lean to the right side. This affects the asymmetric pressure distribution on the surface and the large local side force. Near the position of the minimum local side force (Fig. 8b $x/D = 7.0$), the position of the flow separation at the left side is pulled down and a roughly symmetric pressure distribution is seen. These asymmetric flow characteristics may cause a difference in the local side force. The circumferential surface pressure distributions at the axial positions of $x/D = 3.5$ and 7.0 that are computed through the asymmetric laminar–turbulent transition condition of case 3 are shown in Fig. 9. In the axial position $x/D = 3.5$ a significant asymmetry is seen when compared with the position $x/D = 7.0$. Figure 10 shows the total pressure contours at several cross sections along the body. The asymmetry of the crossflow structure greatly changes between the axial positions of $x/D = 3.5$ and 7.0.

C. Effects of the Angle of Attack

Figure 11 shows comparisons of the normal-force coefficients and the side-force coefficients at different angles of attack. The laminar–turbulent transition conditions are set on the basis of a 50 deg angle of attack (Table 5). The side-force pattern is changed from one of gradual increase to decrease at excessively high angles of attack. This is a well-known phenomenon.

Figure 12 shows a comparison of the local side-force coefficient distributions at various angles of attack for the laminar–turbulent transition condition of case 3-1. The variation of the local side-force distribution is highly irregular. However, at higher angles of attack, the position of the maximum magnitude of the local side force approaches the forebody. This means that the effect of asymmetry is concentrated near the forebody at higher angles of attack. Further, the forebody greatly affects the characteristics of the asymmetric side force and flow patterns.

IV. Conclusions

In this study, the asymmetric flow and side-force characteristics were developed by applying artificially different asymmetric laminar–turbulent transition conditions. The effects of various laminar–turbulent transition conditions and angles of attack are examined. The conclusions in this study are as follows.

1) The results of numerical simulation that are obtained from asymmetric laminar–turbulent transition conditions can yield patterns of the local side-force coefficient distribution and magnitudes of the normal and side forces that are similar to those of experimental findings. It is confirmed that the asymmetries of flow characteristics and forces may be caused by the turbulence effect in the subsonic condition.

2) The magnitude and characteristics of the side force on a flight vehicle are sensitive to the factors of the laminar–turbulent transition model. The starting position and the length of the laminar–turbulent transition may control the asymmetric flow pattern and the side force.

3) The laminar–turbulent transition greatly affects the characteristics of the asymmetric side force and the flow pattern. The asymmetric patterns of flow separations and surface pressure distributions change from the junction of the forebody and the cylinder body.

4) The effects of the angle of attack are studied by the use of modified laminar–turbulent transition conditions that are based on the 50 deg angle-of-attack condition. At higher angles of attack, the position of the maximum magnitude of the local side force approaches the forebody. This means that the effect of the forebody greatly affects the characteristics of the asymmetric side force and the flow pattern.

Acknowledgment

This research was supported by research grants from Yeungnam University in 2007.

References

[1] Nelson, R. C., and Malcolm G. N., "Visualization of High-Angle-of-Attack Flow Phenomena," *Tactical Missile Aerodynamics: General Topics*, Progress in Astronautics and Aeronautics, AIAA, Washington, D.C., 1992, pp. 195–250.

[2] Ericsson, L. E., and Reding, J. P., "Asymmetric Flow Separation and Vortex Shedding on Bodies of Revolution," *Tactical Missile Aerodynamics: General Topics*, Progress in Astronautics and Aeronautics, AIAA, Washington, D.C., 1992, pp. 391–452.

[3] Patel, M. P., Prince, T. S., Carver, R., DiCocco, J. M., Lisy, F. J., and Ng, T. T., "Deployable Flow Effectors for Phantom Yaw Control of Missiles at High Alpha," *Flow Control Conference*,2002-2827, AIAA, Washington, D.C., June 2002.

[4] Keener, E. R., and Chapman, G. T., "Onset of Aerodynamic Side Forces at Zero Sideslip on Symmetric Forebodies at High Angles of Attack," *Mechanics and Control of Flight Conference*, AIAA, New York, Aug. 1974, pp. 1–10; also AIAA Paper 74-770.

[5] Ross, H. M., and O'Rourke, M. J., "Exploratory Investigation of Forebody Strakes for Yaw Control of a Generic Fighter with a Symmetric 60° Half-Angle Chine Forebody," NASA Paper 3604, 1997.

[6] Hunt, B. L., "Asymmetric Vortex Forces and Wakes on Slender Bodies," AIAA, Paper 1982-1336, Aug. 1982.

[7] Chin, S., Lan, C. E., and Gainer, T. G., "Calculation of Asymmetric Vortex Separation on Cones and Tangent Ogives Based on a Discrete Vortex Model," *AIAA Journal*, Vol. 27, No. 12, 1989, pp. 1824–1826. doi:10.2514/3.10342

[8] Lamont, P. J., "Pressure Measurements on an Ogive-Cylinder at High Angles of Attack with Laminar, Transitional or Turbulent Separation," AIAA, Paper 1980-1556, Aug. 1980.

[9] Ericsson, L. E., and Reding, J. P., "Vortex-Induced Asymmetric Loads in 2-D and 3-D Flows," AIAA, Paper 1980-181, Jan. 1980.

[10] Reding, J. P., and Ericsson, L. E., "Maximum Vortex-Induced Side Force Revisited," AIAA, Paper 1983-458, Jan. 1983.

[11] Lombard, C. K., Bardina, J., Venkatapathy, E., and Oliger, J., "Multi-Dimensional Formulation of CSCM an Upwind Flux Difference Eigenvector Split Method for the Compressible Navier–Stokes Equations," *6th Computational Fluid Dynamics Conference*, AIAA, New York, July 1983, pp. 649–664.

[12] Kim, S. D., Kwon, C. O., and Song, D. J., "Comparison of Turbulence Models in Shock-Wave/Boundary-Layer Interaction," *KSME International Journal*, Vol. 18, No. 1, 2004, pp. 153–166.

doi:10.1007/BF03028800

[13] Seo, J. I., Kim, S. D., and Song, D. J., "A Numerical Study on Passive Control of Shock Wave/Turbulent Boundary Layer in a Supersonic Compressor Cascade," *International Journal of Rotating Machinery*, Vol. 8, No. 6, 2002, pp. 423-430. doi:10.1155/S1023621X02000404

[14] Oh, T. H., Kim, S. D., and Song, D. J., "A Numerical Analysis of Transonic/Supersonic Flows in Main Nozzle of Air Jet Loom," *Textile Research Journal*, Vol. 71, No. 9, 2001, pp. 783–790.

[15] Kwon, C. O., Seo, J. I., Bai, C. H., and Song, D. J., "A Computational Study of Two-Dimensional/Axisymmetric Nonequilibrium Chemically Reacting Flows Using Upwind Navier–Stokes Method," *Computational Fluid Dynamics Journal*, Vol. 10, No. 1, 2001, pp. 14–21.

[16] Song, D. J., Kim, S. D., Kwon, C. O., and Seo, J. I., "A Computational Off-Design Performance Analysis of Centrifugal Compressor Diffusers," *Computational Fluid Dynamics Journal*, Vol. 6, No. 9, 1998, pp. 549–560.

[17] Roe, P. L., "Approximate Riemann Solvers, Parameter Vectors and Difference Schemes," *Journal of Computational Physics*, Vol. 43, No. 2, 1981, pp. 357–372. doi:10.1016/0021-9991(81)90128-5

[18] Gostelow, J. P., Blunden, A. R., and Walker, G. J., "Effect of Free-Stream Turbulence and Adverse Pressure Gradients on Boundary Layer Transition," *Journal of Turbomachinery*, Vol. 116, No. 3, 1994, pp. 302–404. doi:10.1115/1.2929426

[19] Champigny, P., "Reynolds Number Effect on the Aerodynamic Characteristics of an Ogive-Cylinder at High Angles of Attack," AIAA, Paper 1984-2176, Aug. 1984.

R. Kimmel
Associate Editor